Brownian dynamics of double-stranded DNA in periodic systems with discrete salt

Steven P. Mielke,[1,][*] Niels Grønbech-Jensen,[2] and Craig J. Benham[1]

[1]*UC Davis Genome Center, University of California, Davis, California 95616, USA*
[2]*Department of Applied Science, University of California, Davis, California 95616, USA*
(Received 2 May 2007; revised manuscript received 20 December 2007; published 31 March 2008)

Numerical models of mesoscale DNA dynamics relevant to *in vivo* scenarios require methods that incorporate important features of the intracellular environment, while maintaining computational tractability. Because the explicit inclusion of ions leads to electrostatic calculations that scale as the square of the number of charged particles, such models typically handle these calculations using low-potential, mean-field approaches, rather than by considering the discrete interactions of ions. This allows approximation of the long-range, screened self-repulsion of DNA, but is unable to capture detailed electrostatic phenomena, such as short-range attractions mediated by ion-ion correlations. Here, we develop a dynamical model of explicitly double-stranded, sequence-specific DNA in a bulk environment consisting of other polyions and explicitly represented counterions and coions. DNA is represented as two interwound chains of charged Stokes spheres, and ions as free, monovalently charged Stokes spheres. Brownian dynamics simulations performed at salt concentrations of 0.1, 1, 10, and 100 mM demonstrate this model captures anticipated behaviors of the system, including increasing compaction of the polyion by the ionic atmosphere with increasing ionic strength. The decay of the distance dependence of the ion concentrations as one moves away from the polyion approaches their equilibrium values in quantitative agreement with predictions of Poisson-Boltzmann theory. The simulation results also demonstrate quantitative agreement with experimental measurements of the persistence length of B-DNA, which increases significantly at low ionic strengths. The model also captures behaviors intimating the importance of explicitly representing ionic and polyionic structure. These include penetration of the polyion interior by both coions and counterions, and counterion-mediated accumulation of coions near the surface of the polyion. Such phenomena are likely to play an important role in the formation of alternative DNA secondary structures, suggesting the present methods will prove valuable to dynamic models of superhelical stress-induced DNA structural transitions.

I. INTRODUCTION

Biological events involving large-scale structural deformations of DNA occur on microsecond and longer time scales. An example of such an event is localized, superhelicity-induced melting of the double helix, in which the topological stress associated with a linking number deficit (underwinding relative to the helicity of relaxed double-stranded DNA [dsDNA]) disrupts base pairing, leading to strand separation at locations (such as gene promoters and origins of replication) where it is potentially required for regulatory function [1–4]. Dynamic modeling of such events requires methods capable not only of following their long-time evolution, but also of accurately capturing biophysical features of the physiological environment within which they occur. These features include interactions with a dielectric solvent at finite temperature, and the presence of both free ions and other charged macromolecules.

One method for modeling large-scale, long-time structural changes in DNA is Brownian dynamics simulation. Brownian dynamics algorithms are based on expressions derived from integrating Langevin equations of motion in the limit of overdamping, where the relaxation time is much smaller than the integration time step. These expressions capture coupling of the system to a heat bath via the fluctuation-dissipation

theorem, which ensures that stochastic fluctuations of particle positions arising from thermal buffeting by solvent molecules correctly correlate with particle velocity dissipation [5]. In this formulation, biopolymers must be idealized as chains of large (relative to implicitly represented solvent molecules), hydrodynamic objects, which are typically modeled as Stokes spheres, or "beads," that interact both locally (via potentials reflecting linear elasticity and excluded volume interactions) and nonlocally (via potentials reflecting long-range electrostatic interactions). In the case of DNA, this approach has been invoked to study a wide range of phenomena, including the effect of intrinsic curvature on ring closure [6], the role of superhelicity in site juxtaposition prior to recombination [7], and the mechanical response of torsionally constrained DNA to dynamically imposed superhelicity [8–10].

To minimize computational cost, Brownian dynamics simulations that model DNA in solution commonly calculate electrostatic interactions using Debye-Hückel theory [6,11,7,12], which arises from linearization of the Poisson-Boltzmann equation when the electrostatic potential energy is much smaller than the Boltzmann energy, $qU \ll k_B T$. (Here, q is charge, U is electric potential, k_B is Boltzmann's constant, and T is the temperature.) Because DNA is highly charged, this requires renormalization of Debye-Hückel potentials so they agree with nonlinear Poisson-Boltzmann theory for simple geometries at large distances (see, for example, Ref. [11]). By assuming that pair interactions between segments of DNA resemble those between charged, colloidal

———————
[*]Author to whom correspondence should be addressed.

cylinders surrounded by a Gouy double layer [13], this renormalized Debye-Hückel approach (and mean-field approaches generally) allow mesoscale DNA models to approximate long-range repulsive forces, but cannot account, e.g., for attractive forces, such as those due to correlations in the positions of ions [14,15]. Such phenomena can only be captured through a discrete-particle representation of ionic species.

Here, we describe methods for simulating the Brownian dynamics of double-stranded DNA in a bulk environment containing both free ions and other polyions (represented as identical images in a periodic lattice). In the present model, the former are represented explicitly as positively or negatively charged, monovalent Stokes spheres in quantities sufficient both to balance the negative polyion (DNA) charge, and to produce electrolytic environments of specified ionic strength. (In what follows, we will refer to the modeled DNA alternately as "DNA," a "macroion," or a "polyion.") DNA is represented as an explicitly double-helical object using an hydrophobic potential that permits specification of base sequence and a detailed account of topological stress [9,10]. The counterions, coions, and polyions occupy a cuboid simulation box under periodic boundary conditions. Long-range electrostatic interactions between particles in the unit cell (simulation box) and those in a lattice of image systems are evaluated using a Lekner summation strategy that allows for accurate, efficient calculation of force expressions and interaction energies [16]. Results from simulations at salt concentrations spanning four orders-of-magnitude, including physiological, demonstrate the capacity of the model to provide reliable mechano-dynamical information about both DNA and the electrolytes with which it interacts in solution.

II. METHODS

A. Explicitly double-stranded DNA model

As was done in previous work [9,10], each of the two interwound polynucleotide strands of DNA was represented as a segmented chain with Stokes spheres (beads) of radius $R_C = 6.5$ Å placed at its vertices to capture hydrodynamic properties (refer to Fig. 1). In the simulations discussed here, the number of beads in each chain was chosen to be $N = 50$. Then the midpoints between the centers of (touching) complementary beads define a central axis with $N-1 = 49$, 10.2 Å (three-base-pair) segments, so the entire structure corresponds to about 147 base pairs (bp) of B-DNA.

Interbead interaction potentials are described in detail in Refs. [9,10]. To review, intrachain particles interact via elastic stretching and bending potentials, interchain particles interact via an hydrophobic potential that allows specification of base sequence, and all particles interact via an excluded volume potential that prevents intrachain and interchain self-passage events. In Refs. [9,10], which omit electrostatic interactions, the total interaction potential for the $2N$ chain particles is given by the expression
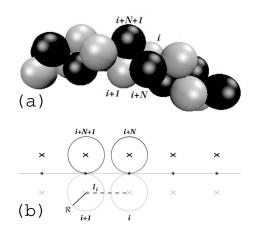

FIG. 1. Double-chain model. (a) Three-dimensional representation of the interwound bead chains. One DNA polynucleotide is black and the other gray. The particles comprising the ith duplex unit are labeled. (b) Corresponding two-dimensional schematic. Complementary beads (e.g., i and $i+N$) touch—i.e., are separated by 2 times the bead radius, R—at mechanical equilibrium. The intrachain separation of particles i and $i+1$ is labeled as l_i. In the three-dimensional structure, noncomplementary interchain beads (e.g., i and $i+N+1$) approximately touch at equilibrium.

$$
U_{\text{Chain}} = \sum_{i=1}^{N-1} U_s(l_i) + \sum_{i=1}^{N-2} U_b(\beta_i) + \sum_{i=N+1}^{2N-1} U_s(l_i) + \sum_{i=N+1}^{2N-2} U_b(\beta_i)
$$

$$
+ U_{\text{ic}}(r_{1,N+2}) + \sum_{i=2}^{N-1} \left[U_{\text{ic}}(r_{i,i+N-1}) + U_{\text{ic}}(r_{i,i+N+1}) \right]
$$

$$
+ U_{\text{ic}}(r_{N,2N-1}) + \frac{1}{2} \sum_{j \neq i=1}^{2N} \sum_{i=1}^{2N} U_{\text{ev}}(r_{ij}). \tag{1}
$$

The individual contributions to this potential are

$$
U_s(l_i) = \frac{K}{2}(l_i - l_0)^2, \tag{2}
$$

$$
U_b(\beta_i) = \frac{A}{2}(\beta_i - \beta_0)^2, \tag{3}
$$

$$
U_{\text{ic}}(r_{ij}) = -\varepsilon_{\text{ic}} \frac{\Delta G_{\text{den}}}{2} \left(\frac{1}{\exp\left[20\left(\frac{r_{ij}}{\sigma_{\text{ic}}} - 1.9 \right) \right] + 1} \right), \tag{4}
$$

$$
U_{\text{ev}}(r_{ij}) = \begin{cases} \varepsilon_{\text{ev}}\left[\left(\frac{\sigma_{\text{ev}}}{r_{ij}} \right)^{12} - \left(\frac{\sigma_{\text{ev}}}{r_{ij}} \right)^{6} \right] + \frac{\varepsilon_{\text{ev}}}{4}, & r_{ij} < \sigma_{\text{ev}} \sqrt[6]{2}, \\ 0, & r_{ij} \geq \sigma_{\text{ev}} \sqrt[6]{2}. \end{cases} \tag{5}
$$

Here, Eq. (2) expresses the potential energy associated with elastic stretching of intrachain segments, $l_i \equiv |\mathbf{r}_{i+1} - \mathbf{r}_i|$ is the length of segment i, and $l_0 = 14$ Å is the equilibrium separation of intrachain particles. The stretching force constant is assumed to be given by $K = k_B T / \delta^2$, where $k_B T$ is the thermal energy (T was set at 293 K) and δ corresponds to the fluc-

tuation of the average segment length (we used the value $\delta = 0.025l_0$ in accordance with previous work [17,8,9]). Equation (3) expresses the potential energy associated with elastic bending of intrachain segments. The angle $\beta_i \equiv \cos^{-1}(\mathbf{r}_{i+2} - \mathbf{r}_{i+1}/|\mathbf{r}_{i+2} - \mathbf{r}_{i+1}| \cdot \mathbf{r}_{i+1} - \mathbf{r}_i/|\mathbf{r}_{i+1} - \mathbf{r}_i|)$ represents the deviation of segment $i+1$ from colinearity with segment i. Bending is assumed to be isotropic, with $\beta_0 = 0$, for all segments. The bending force constant is assumed to be given by $A = k_B T P_{ss}/l_0$ [18], where $P_{ss} = 12.7$ Å is the persistence length of single-stranded DNA [19].

Equation (4) [20] is an expression for the potential energy associated with the hydrophobicity-driven stacking and base pairing of two polynucleotides to form double-stranded DNA. For a given particle, say i in one chain, the interchain potential is given by the sum of pairwise interactions with particles $(i+N)-1$ and $(i+N)+1$ in the other. Then components of the force parallel to the molecular axis are assumed to correspond to stacking forces, and those transverse to the axis to H-bonding forces. Examination of Eq. (4) shows that $U_{ic}(r_{ij}) \sim -\varepsilon_{ic}\Delta G_{den}/2$ for $r_{ij} < 1.6\sigma_{ic}$ and $U_{ic}(r_{ij}) \sim 0$ for $r_{ij} > 2.2\sigma_{ic}$, where r_{ij} is the distance between particles i and j. The parameter σ_{ic} is determined by $1.6\sigma_{ic} = 13.0$ Å, the interchain equilibrium separation of noncomplementary neighbor beads (i.e., beads i and $i+N+1$, or i and $i+N-1$). The factor ΔG_{den} in Eq. (4) is the free energy of local denaturation, as characterized by Benham et al. [2,3]. In the present context, the free energy of denaturation associated to each 3-bp duplex unit is given by

$$\Delta G_{den}(a,b) = a + \sum_{i=1}^{3} b_i, \qquad (6)$$

where a is the free energy needed to nucleate the strand separation transition, and b is the free energy needed to separate the ith base pair. In the investigation reported here, we used the approximately sequence-independent value $a = 10.2$ kcal/mol [3], and the copolymeric value appropriate for $G+C$ base pairs, $b = 1.73$ kcal/mol, for all base pairs, making all model structures $G+C$ copolymers. Because the structures were unconstrained, no stress-induced melting (deviation from equilibrium secondary structure) was observed. The presence of this term enables the analysis of constrained DNA in future studies.

Equation (5) is an expression for excluded volume potential energy, which prevents the overlap and interpassage of both neighbor and non-neighbor intrachain and interchain bead pairs, thereby preserving the topological constraint. The parameter σ_{ev} is determined by $2R_C = \sigma_{ev}\sqrt[6]{2}$, where $\sigma_{ev}\sqrt[6]{2}$ is the pairwise separation corresponding to the minimum of $U_{ev}(r_{ij})$, and R_C is the bead radius. We impose the cutoff, $U_{ev}(r_{ij}) = 0$ for $r_{ij} \geq \sigma_{ev}\sqrt[6]{2}$, so that the potential is strictly repulsive. Consistent with Ref. [9], ensuring that the model DNA maintains a stable double-helical structure that is linear when relaxed requires setting $\varepsilon_{ev}/\varepsilon_{ic} \sim 10^{-8}k_B T$.

The main focus of the present work is the addition of explicit electrostatic interactions to this model. The methods by which this was achieved are described next.

B. Electrostatic interactions with periodic boundary conditions

Electrostatic interactions within a bulk environment were included by defining simulation boxes containing free ions and one free (unconstrained) 50-mer of model DNA, imposing periodic boundary conditions, and then invoking a summation strategy for calculating long-range (Coulomb) forces in periodic systems [16]. Ions were explicitly represented as spheres of radius $R_I = 4$ Å (to account for hydration), at the centers of which were placed the monovalent charges $\pm e$, where e is the elementary charge. We note that ion size can influence the outcome of electrostatic interactions in discrete-particle simulations, but point out that, $R_I = 4$ Å is within the range of experimentally known values for hydrated, monovalent ions, and the results discussed below are in good agreement with experimental data and theoretical predictions. For all interactions, the dielectric constant (see also Sec. II E) was set at the value appropriate for water at 293 K: $D = D_{H_2O} = 4\pi\epsilon_{H_2O}\epsilon_0 = 8.923 \times 10^{-9}$ C^2 N^{-1} m^{-2}, where we have assumed uniform $\epsilon_{H_2O} = 80.2$.

The volumes of the simulation boxes (unit cells defining the lattices of periodic image systems), and the numbers of counterions and coions, were chosen so as to allow simulations at four bulk concentrations: 0.1 mM, 1 mM, 10 mM, and 100 mM. Here and throughout, the bulk (or characteristic) concentration (or ionic strength) is taken to refer to the concentration of 1:1 salt characterizing the volume occupied by the corresponding box, and is assumed to represent the salt concentration that would characterize the solution in the absence of macroions. We note that the ionic strength is equal to the molar concentration for 1:1 salt solutions. Simulations at 0.1 mM required 107 1:1 salt particles (i.e., 107 counterions + 107 coions = 214 total ions) in a cuboid unit cell with sides of length $L_x = L_y = L_z = 1210$ Å. Simulations at 1 mM required 100 1:1 salt particles (200 total ions) in a unit cell with sides of length $L_x = L_y = L_z = 550$ Å. Simulations at 10 mM required 250 1:1 salt particles (500 total ions) in a unit cell with sides of length $L_x = L_y = 275$ Å, $L_z = 550$ Å. Simulations at 100 mM required 2500 1:1 salt particles (5000 total ions) in a unit cell with sides of length $L_x = L_y = 275$ Å, $L_z = 550$ Å.

In addition to the ions required for salt, electroneutrality of the system requires counterions in a quantity sufficient to balance the negative polyion charge, $-294e$ ($2N = 100$ beads at $-5.88e$ per bead, or $-6e$ per three-base-pair axis segment) for all simulations. Therefore, in each case, 294 extra counterions were included. As might be anticipated, these additional ions lead to an overestimation of bulk counterion concentrations within the simulation boxes. This issue is addressed further in Secs. III and IV.

C. Simulation method

Dynamic evolution of the system was described by Brownian dynamics [21],

$$\gamma_i \frac{d\mathbf{r}_i(t)}{dt} = \mathbf{F}_i\{[\mathbf{r}(t)]\} + \mathbf{F}_i'(t). \qquad (7)$$

Here, $\mathbf{r}_i(t)$ is the position and γ_i is the isotropic friction coefficient of the ith particle; $\mathbf{F}_i\{[\mathbf{r}(t)]\}$ is the total deterministic

force acting on particle i due to the positions $[\mathbf{r}(t)]$ of all the particles; and $\mathbf{F}'_i(t)$ is a random force acting on particle i due to its interaction with the heat bath. For particles i and j, this random force is characterized by the fluctuation-dissipation theorem as [5]

$$\langle \mathbf{F}'_i(t) \rangle = 0, \qquad (8)$$

$$\langle \mathbf{F}'_i(0) \cdot \mathbf{F}'_i(t) \rangle = 6\gamma_i k_B T \delta(t) \delta_{ij}. \qquad (9)$$

The friction coefficient can be related to the translational diffusion constant, D_t, according to the Stokes-Einstein relation, $D_{t,i} = k_B T / \gamma_i$, where $\gamma_i = 6\pi\eta R_i$, in which η is the solvent viscosity, and R_i is the particle radius (R_C or R_T). One integration scheme for the resulting equation yields an iterative procedure for the Brownian dynamics of system particles,

$$\mathbf{r}_i(t + \delta t) = \mathbf{r}_i(t) + \frac{D_t}{k_B T}\mathbf{F}_i\{[\mathbf{r}(t)]\}\delta t + \mathbf{S}_i(\delta t). \qquad (10)$$

Here, $\mathbf{S}_i(\delta t)$ is a random Gaussian displacement with $\langle \mathbf{S}_i \rangle = 0$ and $\langle \mathbf{S}_i^2 \rangle = 6D_t \delta t$, and δt is the time step. The deterministic force was obtained from the interaction potentials. The degree of discretization required for numerical stability was determined by the curvature of the potential characterizing charged, finite-size particle collisions. For purposes of calculating excluded volume forces, because the corresponding interactions are relevant only to particles in close proximity, a cell indexing procedure was implemented.

All simulations began with 294 counterions in a uniform configuration surrounding the macroion, aligned along the z axis at the center of the simulation box. At each ionic strength, after this counterion-only system was iterated $\sim 10^7$ times, an appropriate number of coions and additional counterions was randomly distributed throughout the box. Finally, the systems inclusive of both salt and 294 surplus counterions were iterated until the time-averaged concentrations of ions surrounding the macroion were approximately constant (see below). The additional number of iterations required was approximately 2.2×10^7 in the 0.1 mM case, 2.0×10^7 in the 1 mM case, 4.0×10^6 in the 10 mM case, and 2.0×10^6 in the 100 mM case.

Because their calculation significantly increases computation time, hydrodynamic interactions were omitted from the simulations reported here. Since these simulations sample equilibrium phase space, where system configurations depend only on the temperature and the potential energy surface, omission of these interactions does not affect the present results. However, previous work in the context of superhelical DNA has suggested hydrodynamic interactions may facilitate writhing deformations [11,22], indicating that these interactions likely play an important role in nonequilibrium phenomena, such as the mechanical response of DNA to dynamically imposed superhelical stress.

D. Radial distance-dependent salt concentrations

To characterize the spatial distributions assumed by ions relative to the finite, approximately cylindrical macromol-
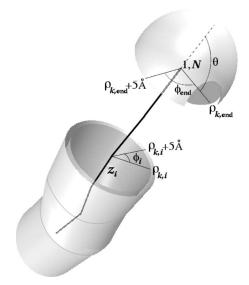

FIG. 2. Volume elements. Volume elements used to obtain radial counterion distributions are represented by gray surfaces. These were defined with respect to local coordinate frames ascribed to the duplex axis (black line) vertices and end points (see Sec. II). To vertex i are associated radial ($\rho_{k,i}$), axial (z_i), and azimuthal (ϕ_i) cylindrical coordinates, where k indexes the volume elements, and an ion is associated to the kth element if its position, $\mathbf{r}$, with respect to the local frame satisfies $[0 < r_{z_i} < 10.2$ Å; $\rho_k < r_{\rho_i} < \rho_k + 5$ Å; $0 < r_{\phi_i} < 2\pi]$. Similarly, to the end points (duplex midpoints 1 and N) are associated radial ($\rho_{k,\mathrm{end}}$), azimuthal (ϕ_{end}), and polar (θ) spherical coordinates, where k again indexes the volume elements, and an ion is associated to the kth element if its position with respect to the local frame satisfies $[-\pi/2 < r_\theta < \pi/2$; $\rho_k < r_{\rho_{\mathrm{end}}} < \rho_k + 5$ Å; $0 < r_{\phi_{\mathrm{end}}} < 2\pi]$.

ecule, at each ionic strength we calculated the time-averaged concentrations of both counterions and coions versus radial distance from the molecular central axis. For this purpose, we first separately calculated the time-averaged numbers of counterions and coions in annular shells of volume, centered at the axis segments, over a range of radial distances. Specifically, for each configuration generated by each of the simulations described above, we first defined orthonormal local coordinate systems at the midpoints between complementary particles in the double-chain; i.e., at the vertices and end points of the discretized central axis. These systems consisted of the normal vectors, $\hat{\mathbf{a}} \equiv (\mathbf{r}_{\mathrm{mid},i+1} - \mathbf{r}_{\mathrm{mid},i})/ |\mathbf{r}_{\mathrm{mid},i+1} - \mathbf{r}_{\mathrm{mid},i}|$, $\hat{\mathbf{b}} \equiv (\mathbf{r}_{i,i+N} \times \mathbf{a})/|\mathbf{r}_{i,i+N} \times \mathbf{a}|$, and $\hat{\mathbf{c}} \equiv [\mathbf{b} \times (-\mathbf{a})]/|\mathbf{b} \times (-\mathbf{a})|$, where $\mathbf{r}_{\mathrm{mid},i}$ is the position of the ith complementary bead-pair midpoint. The vector $\hat{\mathbf{a}}$ was then chosen as the local z direction, the vector $\hat{\mathbf{b}}$ as the local x direction, and the vector $\hat{\mathbf{c}}$ as the local y direction for purposes of transforming into cylindrical coordinates, which allowed counting of ions in annular regions at 5-Å radial intervals about each axis segment, as follows (refer to Fig. 2). The positions, $\mathbf{r}_j$, of all ions were calculated in each local coordinate frame. If a position satisfied $[0 < r_{z,j} < 10.2$ Å; $\rho_k < r_{\rho,j} < \rho_k + 5$ Å; $0 < r_{\phi,j} < 2\pi]$—where z, ρ, and ϕ are its axial, radial, and azimuthal cylindrical components, respectively, and the index k begins at zero ($\rho_0 = 0$) and runs in 5-Å increments out to approximately $L_x/2$—the number of ions

in the corresponding volume shell was incremented by one.

In order to include ions occupying regions at the ends of the polyion, we also counted particles in hemispherical shells of volume centered at the double-chain axis end points in a manner analogous to that in which particles in annular shells were counted; that is, spherical coordinate frames were defined at the end points (refer to Fig. 2), the positions, $\mathbf{r}_j$, of all previously uncounted particles were obtained, and, if position j is satisfied $[-\pi/2 < r_{\theta,j} < \pi/2;\ \rho_k < r_{\rho,j} < \rho_k + 5$ Å; $0 < r_{\phi,j} < 2\pi]$—where θ, ρ, and ϕ are polar, radial, and azimuthal spherical components, respectively, and the index k begins at zero ($\rho_0 = 0$) and runs in 5-Å increments out to approximately $L_x/2$—the number of ions in the corresponding volume shell (associated with segment 1 or $N-1$) was incremented by one.

To include any ions omitted by segmented-cylindrical and spherical counting, we assigned all remaining uncounted particles to the 5-Å volume shell associated with the chain segment to which they were nearest, and within which the distance of nearest approach lay. It was verified for every calculation that exactly the number of ions present was counted. From these axis location-dependent counts, we calculated the total numbers of counterions and coions in all volume shells at each radial distance out to the value of $L_x/2$ appropriate to the simulation under consideration.

Next, to obtain approximate distance-dependent concentrations, we divided these total counts at 5-Å intervals by the volumes $[2\pi r(500$ Å$)(5$ Å$) + 4\pi r^2(5$ Å$)]$, where r is the radial distance; i.e., we divided by the volumes corresponding to perfectly cylindrical shells of 500-Å length (the contour length of the polyion when straight) and 5-Å thickness, plus the volumes corresponding to two hemispherical end shells of 5-Å thickness. Finally, these concentrations were time-averaged over the last 1×10^6 configurations of each simulation. We reiterate that the resulting concentrations are only approximate, because the volumes bounding the deformable polyion are of course unlikely to be perfectly cylindrical in any given configuration. Nevertheless, it is assumed that the time-averaged values represent the concentrations with reasonable accuracy. Moreover, the relative values among the simulations (see below) are expected to be unaffected by the approximation, because they were calculated by the same procedure in all cases. Discrepancies in the ion counts arising from overlap of individual (segmental) volume elements are also not expected to affect the concentration calculations, since the latter depend only on the total number of ions at a given radial distance (and not on specifically which annular elements the ions are deemed to occupy). Even in cases where this information is important, it is expected that any discrepancies will average out over time; the polyion motion ensures that no elements are systematically favored by the method relative to the other elements.

E. Cylindrically symmetric Poisson-Boltzmann theory

We compared the ion concentrations obtained from the simulation results with numerical solutions of the Poisson-Boltzmann equation obtained using the procedure described in Ref. [23], where the system is assumed to consist of a cylindrical particle of radius a, length $l \gg a$ (negligible end effects), uniformly distributed surface charge Qe, and surface potential ψ_0 immersed in a 1:1 electrolyte solution with dielectric constant D and temperature T. The potential in the ionic atmosphere surrounding the cylinder is assumed to be described by the Poisson-Boltzmann equation for the case of cylindrical symmetry,

$$\frac{1}{x}\frac{d}{dx}\left(x\frac{dy}{dx}\right) = \sinh\ y. \tag{11}$$

Here, $y = e\psi/k_{\mathrm{B}}T$ is the dimensionless potential and $x = \kappa r$ is the dimensionless distance. In the latter expression, r is the radial distance from the center of the cylinder and $\kappa = \sqrt{8\pi e^2 I/Dk_{\mathrm{B}}T}$ is the Debye parameter, for which all values were chosen to be consistent with the simulations: $T = 293$ K, $D = D_{\mathrm{H_2O}} = 8.923 \times 10^{-9}$ C^2 N^{-1} m^{-2}, and the bulk electrolyte concentrations $I = 0.1$ mM, 1 mM, 10 mM, and 100 mM, resulting in the values $\kappa = 0.003\ 280$ Å^{-1}, $0.010\ 37$ Å^{-1}, $0.032\ 80$ Å^{-1}, and 0.1037 Å^{-1}, respectively, for the four simulations. At the cylinder surface, $x = x_0 = \kappa a$ and $y = y_0 = e\psi_0/k_{\mathrm{B}}T$. The radius a was set at 12 Å so that it approximately corresponds to the radius of B-DNA.

At each ionic strength, Eq. (11) was solved using a fourth-order Runge-Kutta procedure with fixed space step, $dx = e^{0.01}$. The boundary conditions were chosen so that the predicted counterion and coion concentrations reached their bulk values at distances that produced a good overall fit to the respective data when the predicted surface potential, ψ_0, agreed with that obtained from the simulations. (For this purpose, a space- and time-averaged potential at a radial distance of 12 Å was calculated.) The predicted concentrations are given by $\varrho = I e^{\varphi y}$ for the counterions and $\varrho = I e^{-\varphi y}$ for the coions, where we have incorporated the cofactor, φ, in order to parametrize the potential to account for differences between the system assumed by the dynamic model and that assumed by the theory. In particular, the former introduces discretization of (both ion and polyion) charge, ion finite size, and polyion finite length (end effects), flexibility, and penetrability; certainly the presence of counterions and coions within the polyion can be expected to alter its "surface" potential. These differences notwithstanding, the simulations and parametrized theory agree quite well in regions where the concentrations are decaying, as shown below. For the counterions, we used the value $\varphi = 1.0$, except in the 100 mM case, in which $\varphi = 0.33$. For the coions, we used the values $\varphi = 0.085$, 0.45, 0.38, and 0.09 in the 0.1, 1, 10, and 100 mM cases, respectively.

F. Persistence lengths

Because we sought to compare our simulation results directly with the experimental results reported in Ref. [24], persistence lengths were calculated using the approximate expression of Hagerman and Zimm [18],

$$R_a = 1.0120 - 0.248\ 13X + 0.033\ 703X^2 - 0.001\ 917\ 7X^3. \tag{12}$$

Here, $R_a = \tau_a/\tau_B$ expresses the ratio of the approximate rotational relaxation time to the Broersma rotational relaxation

time (see below), and $X=L/P$, where L is the molecular contour length (the value $L=500$ Å was used throughout) and P is the persistence length. The approximate rotational relaxation time, τ_a, was calculated according to $1/\tau_a = 3(\langle D_{\hat{x}} \rangle + \langle D_{\hat{y}} \rangle)$, where $\langle D_{\hat{x}} \rangle$ and $\langle D_{\hat{y}} \rangle$ are time-averaged rotational diffusion coefficients obtained from the expression [25]

$$D_{\hat{x}} = \left(\frac{k_B T}{6\pi \eta R_C S_{\hat{x}}} \right)$$
$$\times \left[1 + \left(\frac{3R_C}{4S_{\hat{x}}} \right) \sum_i \sum_{j \neq i} \left(\frac{y_i y_j + z_i z_j}{r_{ij}} + \frac{(y_i z_j - y_j z_i)^2}{r_{ij}^3} \right) \right],$$

(13)

where $S_{\hat{x}} = \Sigma_i (y_i^2 + z_i^2)$, and the appropriate corresponding expressions were used to calculate $D_{\hat{y}}$. In Eq. (13), i and j index the positions of beads in the double-chain relative to a coordinate system whose origin is the center of mass, and whose principal axes diagonalize the inertia tensor. The r_{ij} are separations between bead centers, and the other parameters were defined previously. Our procedure was, for a given configuration generated by the simulations, to calculate the center of mass of the double-chain particles, diagonalize the moment of inertia tensor to define the principal axes, and then calculate $D_{\hat{x}}$ and $D_{\hat{y}}$ using Eq. (13). For each simulation, the diffusion coefficients thus calculated were averaged over the same 1 000 000 configurations used to calculate the averaged, distance-dependent concentrations, and τ_a was then calculated using these $\langle D_{\hat{x}} \rangle$ and $\langle D_{\hat{y}} \rangle$. Next, the Broersma relaxation time was calculated from $1/\tau_B = 6D_B$, where [26]

$$D_B = \left(\frac{3k_B T}{\pi \eta L^3} \right) \left[\ln \frac{L}{b} - 1.57 + 7 \left(\frac{1}{\ln(L/b)} - 0.28 \right)^2 \right].$$

(14)

Here, L is the axial length of the Broersma cylinder, b is its transverse radius, and the other parameters were defined previously. For L we used the value 500 Å, and for b the value 7.5 Å, corresponding to the radius of a cylinder occupying the same volume per unit length as one pair of complementary beads in the double chain. Finally, at each ionic strength, with all other variables determined, Eq. (12) was solved for P.

III. RESULTS

Figures 3(a), 3(b), 3(c), and 3(d) display frames rendered from the 0.1 mM, 1 mM, 10 mM, and 100 mM simulations, respectively, after at least 2.0×10^6 iterations in the presence of salt (see Sec. II). In each case, the periodic simulation cell is represented as a box, with dimensions indicated, and double-helical DNA entirely of $G+C$ content as interwound, black and white bead chains. Counterions and coions are depicted as gray and white spheres, respectively. The sizes of the particles are chosen for clarity, and do not accurately reflect relative scale. In Figs. 3(a)–3(c), a fraction of the ions is seen to associate with the negatively charged macroion, and the remaining ions to be distributed approximately uni-

formly throughout the cell. In the 100 mM case [Fig. 3(d)], the macroion is largely obscured by the counterions and coions. Inspection of the figures additionally reveals that the macroion is significantly straighter in the 0.1 mM case [Fig. 3(a)] than in the 1, 10, and 100 mM cases. This is suggestive of the ionic strength dependence of the persistence length, which will be addressed below.

To characterize the ion spatial distributions, we calculated the time-averaged concentrations of counterions and coions as a function of radial distance from the macroion central axis, as described in Sec. II. Our results are shown in Fig. 4, where Parts (a), (b), (c), and (d) correspond to the 0.1, 1, 10, and 100 mM simulations, respectively (these concentrations are indicated by solid horizontal lines in the figure). The distance axes terminate at one-half the corresponding shortest box dimension, where there is a symmetry point associated with the periodic boundary conditions. Counterion and coion concentrations are distinguished by solid and dashed error bars, respectively. The solid curves in Fig. 4 are concentrations calculated from numerical solutions of the Poisson-Boltzmann equation for the case of cylindrical symmetry, under the boundary conditions described in Sec. II. The dashed vertical lines in the figure indicate end points of these curves at 12 Å (the radius of the charged cylinder assumed by the theory) and at the distances at which the counterion Poisson-Boltzmann curves reach their bulk values. It is assumed that, beyond these distances, analytical solution of the theory would yield concentrations for both counterions and coions that are asymptotically close to their bulk values. The fit between the concentrations predicted by Poisson-Boltzmann theory and those obtained from the simulations is generally quite good in the region intermediate to these points, where simulated concentrations of both counterions and coions are converging from extremal to bulk values.

For both counterions and coions, the theoretical and simulated concentrations deviate at distances just beyond the theory curve end point at 12 Å, which coincides with the excluded volume surface of the dynamic macroion ($2R_C = 13$ Å). This is no doubt primarily a consequence of the ionic penetration of the interior (interstitial) region of the double-helix accommodated by the dynamic model, but not the theory, as evidenced in Fig. 4 by data points (but no predictions from the theory) at distances less than 12 Å. Figure 4 shows that in all cases (within the error) the concentrations of counterions between 0 and 20 Å increase with increasing distance and molarity (ionic strength characterizing the simulation). In all cases, the fourth (15−20 Å) counterion data point underestimates the theoretical concentration, but represents the maximum simulated concentration, with the values 0.130 ± 0.003 M, 0.231 ± 0.003 M, 0.329 ± 0.004 M, and 0.469 ± 0.004 M in the 0.1, 1, 10, and 100 mM cases, respectively. The coion concentrations are seen to reach local maxima between 0 and 15 Å, and to overestimate the theory in the 15−20 Å region. Both the maxima and degree of overestimation increase proportionally with the ionic strength. The values of these local maxima are 0.0524 ± 0.0510 mM, 0.101 ± 0.0979 mM, 5.13 ± 1.04 mM, and 145 ± 3.21 mM at 0.1, 1, 10, and 100 mM, respectively. Certainly the accumulation of coions near
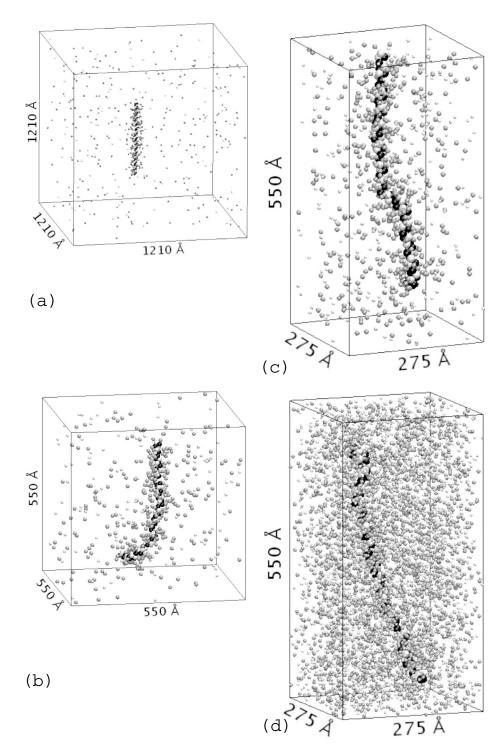
FIG. 3. Configuration snapshots and system geometries. The pictured unit cells (dimensions indicated) correspond to simulations at 0.1 mM (a), 1 mM (b), 10 mM (c), and 100 mM (d) 1:1 salt concentrations. Counterions and coions are represented as gray and white spheres, respectively. In each case, a free, 147 base pair, $G+C$ copolymeric DNA molecule is represented as interwound, black and white bead chains. Relative sizes of the particles are chosen for clarity. All four snapshots were taken after at least 2.0 $\times 10^6$ configurations with salt had been generated.

the surface of (and within) the highly negatively charged macroion is a consequence of the presence of counterions, indicating the potential importance of modeling ions as discrete particles of finite size.

The theoretical and simulated counterion concentrations also deviate where the former terminate at their bulk values, and the latter approach equilibrium values influenced by the additional 294 counterions present in all cases to satisfy electroneutrality. In particular, in the 0.1 mM and 1 mM cases [Figs. 4(a) and 4(b)], where the deviation from bulk values near and beyond the bounding distance of the theory is most apparent (in part because emphasized by the logarithmic scale), the 294 additional counterions alone constitute concentrations of 0.28 mM in the "0.1 mM" simulation [i.e., the simulation with 214 balanced counterions and coions in a box of volume (1210 Å)^3] and 2.9 mM in the "1 mM" simulation [i.e., the simulation with 200 balanced counterions and coions in a box of volume (550 Å)^3]—280% and 290% of the respective assumed bulk values. In the 0.1 mM case, counterion concentrations in this region are characterized by significant fluctuations around a value of approximately 0.2 mM, suggesting the additional ions may generally preclude
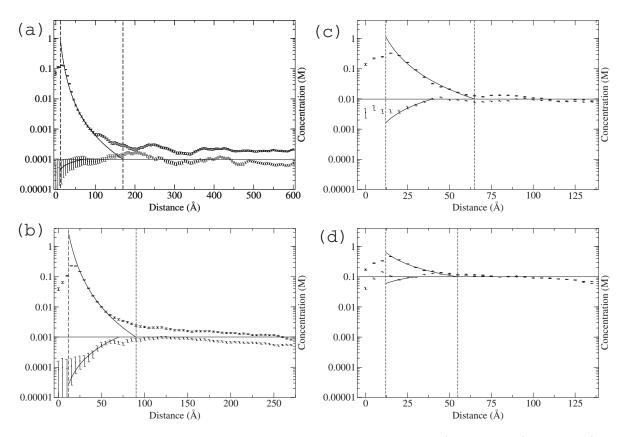
FIG. 4. Salt concentrations versus radial distance. Averaged concentrations of counterions (solid error bars) and coions (dashed error bars) in volume shells of 5-Å radial width surrounding the central macroion are plotted (on logarithmic scale) at radial distances out to the half-width of the simulation boxes. The bulk concentration of 1:1 salt is indicated in each figure by a solid horizontal line: (a), (b), (c), and (d) correspond to the simulations at 0.1 mM, 1 mM, 10 mM, and 100 mM, respectively. The solid curves represent concentrations predicted by numerically solving the Poisson-Boltzmann equation for a cylinder with uniform surface charge density and a radius of 12 Å. This radius, and the distances at which the predicted counterion concentrations reach their bulk values, are indicated by dashed vertical lines. The latter decrease with increasing ionic strength, suggesting that the ionic atmosphere becomes increasingly compact, as anticipated. The simulations overestimate the counterion concentrations in the bulk region owing to the 294 additional counterions required to satisfy electroneutrality.

the simulated counterion concentrations reaching bulk values. In the 1 mM case, the counterion concentrations first decay in this region, and then level off at a value just above 1 mM between 225 and 255 Å, beyond which they taper off (likely as a consequence of symmetry at $L/2$ arising from the periodic boundary conditions [see also Fig. 4(d)]). Although the coion concentrations more closely approximate the assumed bulk values in the distant region, they, like the counterion concentrations, fluctuate. This may be indicative of incomplete sampling of configuration space.

Finally, we point out that the distance at which both counterion and coion concentrations are deemed to have reached their equilibrium values—the bulk boundary of the theory, as determined by fitting to the counterion data—decreases with increasing characteristic ionic strength, having the values 170 Å, 90 Å, 65 Å, and 60 Å in the 0.1, 1, 10, and 100 mM cases, respectively. Both this result, and the observation that the ion concentrations close to the model DNA increase significantly with increasing ionic strength, indicate that the ionic atmosphere enshrouding the DNA generally becomes increasingly compact as salt is added, consistent with the well-known behavior of electrolytes in solution with macro-ions or polyelectrolytes [27].

The foregoing suggests that the simulated ion distributions form three qualitatively distinct regions, indicated by the theory boundaries (dashed vertical lines) in Fig. 4: An interior region occupied by particles that penetrate the effective hydrodynamic surface of the polyion; a near region, within which the concentrations decay from large, ionic strength-dependent values close to the surface to relatively small, equilibrium values at an intermediate distance; and a far region, where the concentrations fluctuate near these values out to the half-width of the simulation cell. We note the similarity between these regions and those characterizing the electrical double-layer model of Schellman and Stigter [28], in which a Stern layer within the hydrodynamic shear surface of DNA (represented as a cylinder with uniform surface charge) is surrounded by a diffuse ionic atmosphere consisting of an inner Gouy layer, where the potential is described by the full, nonlinear Poisson-Boltzmann equation, and an outer Debye-Hückel layer (often associated with the Debye length), where the electrostatic potential has been attenuated to the extent that the Debye-Hückel approximation becomes valid (see Fig. 1 in Ref. [28]).

To begin investigating the effects of discrete ions on the structural properties of DNA in our simulations, we have
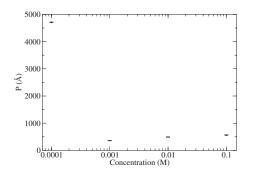
FIG. 5. Persistence lengths. Mean values of the persistence length and their standard deviations calculated from simulations at four salt concentrations, 0.1 mM, 1 mM, 10 mM, and 100 mM (plotted on logarithmic scale). At 1, 10, and 100 mM, $P \approx 500$ Å, in agreement with the familiar value associated to B-DNA. At 0.1 mM, the persistence length is seen to be significantly larger ($P \approx 4700$ Å), consistent with the experimental results described in Ref. [24].

calculated time-averaged persistence lengths of the model polyion at each concentration, as described in Sec. II. Our results are shown in Fig. 5, where it is evident that the calculated values agree well with the generally accepted value for B-DNA ($450-500$ Å) at 1, 10, and 100 mM, and deviate markedly from this value at 0.1 mM. These results are in excellent agreement with the experimental work of Hagerman, which has shown that 587-bp fragments in NaCl have a persistence length of around 1800 Å at 0.1 mM, but maintain a value of around 500 Å at concentrations higher than about 1 mM [24], suggesting there is no significant ionic contribution to the persistence length in this regime of concentrations. Our overestimate of the persistence length at 0.1 mM (4709 ± 15 Å) is consistent with the model polyion being smaller than the DNA fragments used in the experiments; its smaller size renders it more susceptible to stiffening from the self-repulsion of phosphate charges in the regime of concentrations where there is little screening, and ionic contributions to the persistence length are significant. We point out that for longer molecules (e.g., the 40 000-bp T7 DNA used in the experiments reported in Ref. [29]) these contributions are known to extend to higher ionic strengths, likely as a consequence of a more pronounced contribution from excluded volume effects.

IV. DISCUSSION

DNA structural transitions related to underwinding of the double-helix (negative superhelicity) have been implicated in all fundamental biological events involving DNA—the transcription of genes, the replication and recombination of chromosomes, and the repair of DNA damage—in organisms at all levels of complexity [1–4]. The overarching goal of the research effort described here is to provide a reliable and efficient dynamic modeling framework for biologically relevant scenarios involving superhelical DNA. This requires incorporating as many features of the intracellular environment influencing those scenarios as possible, while maintaining computational tractability. An important example of such a feature is long-range electrostatic interactions between free, monovalent and polyvalent ions and highly charged macromolecules. Other dynamic, mesoscale DNA models that capture near-equilibrium effects of superhelicity have included electrostatic interactions using procedures that assume a mean field of ions separates distant, linearly charged segments of a single polymer chain. This approximates long-range, screened self-repulsion of the chain, but does not allow these models to capture effects arising from the presence of discrete ions; for example, the aforementioned ion-ion correlations that can produce attractions between like-charged polyions in close proximity [15], and local effects, such as those due to ionic penetration of the hydrodynamic surface of the polyion, which can play an important role in the formation of alternative secondary structures.

Here, we have sought to incorporate discrete electrostatic interactions into our explicitly double-stranded, sequence-specific model that has previously been shown to be capable of capturing localized, stress-induced melting events within dynamically superhelical DNA molecules. (Because the model DNA used in the present study was unconstrained, the dynamics reported here do not include these events.) Results from Brownian dynamics simulations carried out at salt concentrations spanning several orders-of-magnitude demonstrate that our computational methods yield expected qualitative behaviors of the system; in particular, concentration-dependent association of ions with the polyelectrolyte that includes intrusion into its hydrodynamic interior, and stiffening of the latter in the regime of low ionic strengths, where reduced screening leads to significant phosphate self-repulsion. These results further demonstrate quantitative agreement both with predictions of Poisson-Boltzmann theory and with experimental measurements of the persistence length of B-DNA.

Time-averaged calculations of coion and counterion concentrations versus radial distance suggest that, with increasing ionic strength, the ionic atmosphere associated with the polyion becomes increasingly compact (small and dense), a familiar feature of polyelectrolyte systems. At each ionic strength investigated, both counterion and coion concentrations reach extrema near the hydrodynamic surface, beyond which they decay nonlinearly with increasing distance from the molecular axis in a manner that agrees quantitatively with predictions of cylindrically symmetric Poisson-Boltzmann theory. The behavior of coions near and within the molecular surface—in particular, the ionic strength-dependent elevation of their concentrations—is presumed to be a consequence of their interactions with the highly concentrated counterions, and indicative of the importance of close-range, finite-size effects. Deviations of simulated counterion and coion concentrations from their assumed bulk values in regions where the theory predicts those values (i.e., beyond the large-distance boundaries depicted in Fig. 4), likely arise principally from the over representation of counterions required by the electroneutrality condition. We point out that the periodic boundary conditions fully accommodate "wrapping" of the polyion across the simulation box, which could lead to its self-interaction under some circumstances. This would effectively model the interaction of two polyions

in solution, but also significantly disrupt the free ion distributions. There is no evidence of such an interaction in the regions of configuration space explored by the simulations considered here.

Qualitatively, the simulated ion distributions are characterized by three regions: An interstitial region, containing ions that penetrate the hydrodynamic surface of the model DNA; a near region, within which concentrations decay from extrema near the molecular surface to equilibrium values; and a far region, within which the concentrations fluctuate near these values out to the simulation cell boundary. This indicates that, on average, one fraction of the ions (that defining the interstitial and near regions) associates closely, and another (that defining the far region) more loosely with the polyion. However, the stochasticity inherent to the Brownian system precludes identifying individual ions with either fraction over large regions of phase space. [We compare this situation to that described in Ref. [28], where it is noted that there is no physical basis for separating the ionic atmosphere into Gouy (or "condensed") and Debye-Hückel components.] It is possible that interactions between the macroion and ions of the interstitial region more closely approximate true binding. Because a principal advantage of the present framework is its ability to model structure and dynamics in this region, it will be possible to address this issue in future studies.

In addition to the dynamic behavior of finite-size ions, we have investigated the dynamic and mechanical behavior of explicitly double-stranded DNA in the present model by performing calculations of the persistence length over the same four-order-of-magnitude range of ionic strengths considered for the concentration calculations. At 1, 10, and 100 mM, we obtain values in excellent agreement with the generally accepted value for B-DNA ($450-500$ Å), suggesting the mechanical parameters characterizing DNA in the model accurately capture its bending properties. At 0.1 mM, we obtain the much higher value 4709 ± 15 Å, in approximate agreement with the value of around 1800 Å obtained by Hagerman using longer molecules [24]. These results suggest the model accurately captures ionic contributions to the mechanical properties of DNA arising in the regime of ionic strengths where polyion self-repulsion fails to be attenuated by a high density of ambient counterions. We are currently performing additional simulations to further investigate this effect.

Polyelectrolyte solutions remain a subject of intense investigation, and numerous theoretical descriptions of the ionic atmosphere have been proposed. These include, to name a few, the controversial (see, for example, Refs. [30–33]) Manning condensation model [34–36], the aforementioned Stigter model [23,28,13], cell models [33,37], and Monte Carlo models [38,39]. The methods described here will contribute to this effort by capturing electrical phenomena inaccessible to approaches that either model salt as a mean-field, or model DNA as a line charge or cylinder with uniform surface charge. These phenomena include correlation effects, which depend on the valence and positions of finite-size ions, and occupation by the ions of the interstitial region of double-stranded DNA, where they can, for example, influence the formation of biologically significant alternative secondary structures. The model will also complement ongoing work in other space and time regimes associated with this multiscale problem, such as that reported in Ref. [40]. Extension of the model to scenarios involving longer, torsionally constrained DNA of heterogeneous base sequence will potentially provide dynamic information about important superhelical stress-driven structural changes *in vivo*.

[1] C. J. Benham, Proc. Natl. Acad. Sci. U.S.A. **76**, 3870 (1979).

[2] C. J. Benham, J. Mol. Biol. **225**, 835 (1992).

[3] W. R. Bauer and C. J. Benham, J. Mol. Biol. **234**, 1184 (1993).

[4] C. J. Benham and C. Bi, J. Comput. Biol. **11**, 519 (2004).

[5] G. Parisi, *Statistical Field Theory* (Addison-Wesley, Redwood City, 1988).

[6] H. Merlitz, K. Rippe, K. V. Klenin, and J. Langowski, Biophys. J. **74**, 773 (1998).

[7] J. Huang and T. Schlick, J. Chem. Phys. **117**, 8573 (2002).

[8] S. P. Mielke, W. H. Fink, V. V. Krishnan, N. Grønbech-Jensen, and C. J. Benham, J. Chem. Phys. **121**, 8104 (2004).

[9] S. P. Mielke, N. Grønbech-Jensen, V. V. Krishnan, W. H. Fink, and C. J. Benham, J. Chem. Phys. **123**, 124911 (2005).

[10] S. P. Mielke and V. V. Krishnan, Trends Chem. Phys. **13**, 29 (2006).

[11] K. Klenin, H. Merlitz, and J. Langowski, Biophys. J. **74**, 780 (1998).

[12] G. Arya, Q. Zhang, and T. Schlick, Biophys. J. **91**, 133 (2006).

[13] D. Stigter, Biopolymers **16**, 1435 (1977).

[14] I. Rouzina and V. A. Bloomfield, J. Phys. Chem. **100**, 9977 (1996).

[15] N. Grønbech-Jensen, R. J. Mashl, R. F. Bruinsma, and W. M. Gelbart, Phys. Rev. Lett. **78**, 2477 (1997).

[16] N. Grønbech-Jensen, Int. J. Mod. Phys. C **8**, 1287 (1997).

[17] G. Chirico and J. Langowski, Biopolymers **34**, 415 (1994).

[18] P. Hagerman and B. Zimm, Biopolymers **20**, 1481 (1981).

[19] V. A. Bloomfield, D. M. Crothers, and I. Tinoco, Jr., *Physical Chemistry of Nucleic Acids* (Harper and Row, New York, 1974).

[20] H. Noguchi and M. Takasu, Phys. Rev. E **64**, 041913 (2001).

[21] M. P. Allen and D. J. Tildesley, *Computer Simulations of Liquids* (Oxford, New York, 1987).

[22] S. P. Mielke, Doctoral dissertation, UMI, 2006.

[23] D. Stigter, J. Colloid Interface Sci. **53**, 296 (1975).

[24] P. Hagerman, Biopolymers **20**, 1503 (1981).

[25] J. Garcia de la Torre and V. A. Bloomfield, Biopolymers **16**, 1765 (1977).

[26] S. Broersma, J. Chem. Phys. **32**, 1626 (1960).

[27] R. Gabler, *Electrical Interactions in Molecular Biophysics* (Academic, New York, 1978).

[28] J. A. Schellman and D. Stigter, Biopolymers **16**, 1415 (1977).

[29] V. Rizzo and J. Schellman, Biopolymers **20**, 2143 (1981).

[30] D. Stigter, J. Phys. Chem. **82**, 1603 (1978).

[31] D. Stigter, Biophys. J. **69**, 380 (1995).

[32] R. M. Nyquist, B.-Y. Ha, and A. J. Liu, Macromolecules **32**, 3481 (1999).

[33] P. L. Hansen, R. Podgornik, and V. A. Parsegian, Phys. Rev. E **64**, 021907 (2001).

[34] G. R. Manning, Q. Rev. Biophys. **11**, 179 (1978).

[35] J. Ray and G. R. Manning, Macromolecules **32**, 4588 (1999).

[36] G. R. Manning, Biophys. Chem. **101–102**, 461 (2002).

[37] D. Antypov and C. Holm, Phys. Rev. Lett. **96**, 088302 (2006).

[38] A. Naji and R. R. Netz, Phys. Rev. Lett. **95**, 185703 (2005).

[39] A. Naji and R. R. Netz, Phys. Rev. E **73**, 056105 (2006).

[40] A. Savelyev and G. A. Papoian, J. Am. Chem. Soc. **128**, 14506 (2006).